V European Conference on Computational Fluid Dynamics
ECCOMAS CFD 2010
J. C. F. Pereira and A. Sequeira (Eds)
Lisbon, Portugal, 14–17 June 2010

LARGE EDDY SIMULATION OF JET IN CROSS-FLOW APPLIED TO THE "MICROMIX" HYDROGEN COMBUSTION PRINCIPLE

Elmar Recker[*], Walter Bosschaerts[†], Patrick Hendrick[††]

[*†]Royal Military Academy
Rue de la Renaissance 30, 1000 Brussels, Belgium
e-mail: elmar.recker@rma.ac.be

[††]Université Libre de Bruxelles
Avenue Fr. Roosevelt 50, 1050 Brussels, Belgium
patrick.hendrick@ulb.ac.be

Key words: Jet In Cross-Flow, LES

Abstract. *With the final objective of optimizing the "Micromix" combustion principle, the scalar and velocity field in a round jet in a laminar cross-flow prior to its combustion are computed by Large Eddy Simulations (LES). Simulations were performed at two jet to cross-flow momentum ratios, 5.7 and 1.1, and respective Reynolds number, 5000 and 1600, based on the jet velocity and jet exit diameter. Mean and fluctuating field terms, successfully assessed against experimental and numerical measurements, provide insight into the effect of jet to cross-flow momentum ratio on the formation and evolution of the vortical structures and the associated mixing. From a global viewpoint, the principal vortical systems which are formed are the same for both momentum ratios. The jet/cross-flow mixture converging upon the span-wise centre-line, the lifting action of the Counter Rotating Vortex Pair (CRVP) and the reversed flow region contribute to the high entrainment and mixedness in the downstream region. Specifically the mechanism leading to CRVP differs fundamentally. For r = 5.7, the jet exhibits rollup of vortical structures, in addition to tilting and folding of the evolving open loops. The destabilization is induced by Kelvin-Helmholtz instabilities on the shear layers. At the low r a deep penetration of the cross-flow fluid into the jet core is observed. The jet flow starts to oscillate, the stream-wise CRVP pair, leading to the formation of ring like vortices.*

1 INTRODUCTION

Control of pollutant emissions has become a major factor in the design of modern combustion systems. The "Liquid Hydrogen Fuelled Aircraft – System Analysis" FPS project funded in 2000 by the European Commission can be seen as such an initiative[1]. In the frame of this project, the Aachen University of Applied Sciences (ACUAS) developed experimentally the "Micromix" hydrogen combustion principle and implemented it successfully on the Honeywell APU GTCP 36-300 gas turbine engine. The objectives of the current research are to optimize the burner design by computer simulations. Due to the complex interrelation of chemical kinetics and flow dynamics, the "Micromixing" was analyzed first.

2 MICROMIX HYDROGEN COMBUSTION PRINCIPLE

Lowering the reaction temperature, eliminating hot spots from the reaction zone and keeping time available for the formation of NO_x to a minimum are the prime drivers in NO_x reduction. The "Micromix" hydrogen combustion principle meets those requirements by minimizing the flame temperature working at small equivalence ratios, improving the mixing by means of Jets In Cross-Flow (JICF) and reducing the residence time in adopting a combustor geometry providing a very large number of very small flames uniformly distributed across the burner main cross section (Fig. 1)[2].

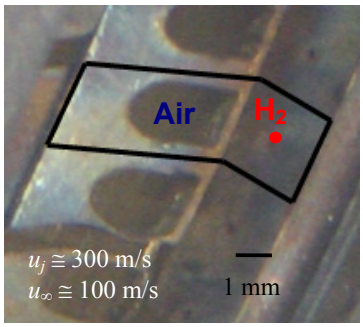

Figure 1: Individual injection zone (courtesy ACUAS).

Compared to the unconverted APU, the NOx emissions are reduced by a ratio 10, confirming the promising innovative "Micromix" combustion principle (Fig. 2)[3].

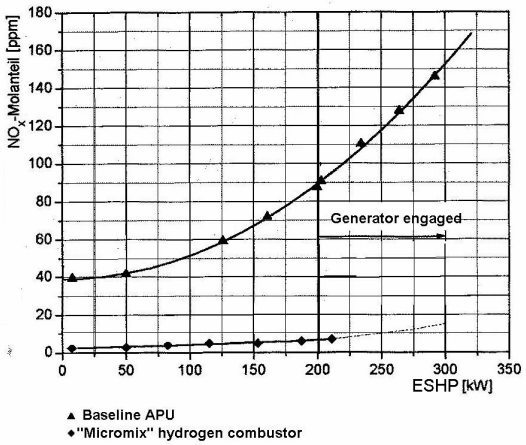

Figure 2: "Micromix" hydrogen combustor emission level (courtesy ACUAS).

3 JETS IN CROSS-FLOW

Jets In Cross-Flow are defined as the flow field where a jet of fluid enters and interacts with a cross-flowing fluid. A jet issuing in the +*y*-direction, into a cross-flow in the +*x*-direction will bend in the stream-wise direction. As the jet bends, fluid is entrained, and vorticity in both the issuing jet and the free-stream stretches and aligns to form four dominant flow structures: Counter Rotating Vortex Pair, leading-edge and lee-side vortices, horseshoe vortex system and wake vortices (Fig. 3)[4].

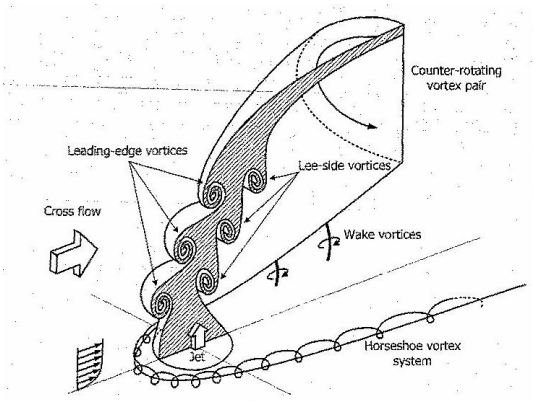

Figure 3: Schematic drawing of the vortical structures in JICF.

The most dominant quantity to characterize a JICF is the momentum ratio defined as:

$$r = \sqrt{\frac{\rho_j \cdot u_j^2}{\rho_\infty \cdot u_\infty^2}} \tag{1}$$

The "Micromixing" JICF operates at a $r \approx 1$, which is low for combustor type mixing. The Reynolds numbers Re_{jet} and $Re_{\text{jet/freestream}}$, based on the jet diameter and jet velocity and on the jet diameter and free-stream velocity, are respectively 930 and 650.

Experimental and numerical investigations of the flow physics of the JICF have been quite plentiful. The bibliographic study is here limited to look at relevant previous investigations. One has to be aware, that the formation of the CRVP is still an open issue. On the one hand, it appears that the destabilization mechanism is *r* dependent. On the other hand, no conclusive *Re* dependence is reported.

Kelso, Lim & Perry (1995)[5] investigated the structure of JICF for *r* ranging from 2 to 6 and $Re_{\text{jet/freestream}}$, in the range of 440 to 6200. Downstream of the jet, there appeared to be a node which resides a short distance downstream of the edge of the nozzle. In addition, they suggested that the destabilization is induced by Kelvin-Helmholtz like instabilities on the shear layers. The evolving vortex rings are thought to tilt and fold, leading to the formation of the CRVP.

For JICF with $r < 1$, Andreopoulos and Rodi (1984)[6] observed jet pipe blockage. Jet bending was seen to start already inside the pipe with some pipe fluid that was observed to be entrained into the horseshoe vortex. Like Kelso, Lim & Perry, they proposed that the CRVP vorticity is generated by the shear between the jet and the cross-flow.

Yuan, Street and Ferziger (1999)[7] performed LES at two *r*, 2 and 3.3, and respective $Re_{\text{jet/freestream}}$ of 1050 and 2100. They identified hanging vortices on the lateral edge and immediately downstream of the jet, providing the necessary circulation to create the CRVP.

Lim, New & Luo (2001)[8] investigated the development of the shear layer vortices of JICF in water by releasing dye around the jet exit. They concluded that the jet shear-layer vortices are open loops that merge into the CRVP. Another important feature is that at $r \leq 1$, the upstream vortices are pointed downstream rather than upstream as is it commonly observed in high r cases.

Those observations are complemented through PIV measurements and flow visualizations by Camussi, Guj and Stella (2002)[9] (r ranging from 1.5 to 4.5 at $Re_{jet} = 100$). They report longitudinal vorticity dominated by wake-like structures. The measurements gave no evidence of Kelvin-Helmholtz induced shear layer roll up. They attributed the instability mechanism to jet oscillation, leading to the pairing of the CRVP and the formation of ring like vortices.

4 FLOW CONFIGURATION

In order to obtain meaningful statements on the validity of the LES computations, test cases are needed which are close to the real problem with respect to Reynolds number and momentum ratio. Unfortunately, no experimental flow field characteristics, close to the real problem, are available. As no scalar field measurement equipment is available, the concentration measurements of Su & Mungal (2004)[10] offer the best option. The flow field is assessed against in house SPIV measurements on an up scaled geometry with a ratio of 1:33, defining r as invariant at representative Re_{jet} and $Re_{\text{jet/freestream}}$.

4.1 Test case of Su & Mungal

Su & Mungal measured the planar scalar mixing in a JICF with $r = 5.7$ and $Re_{\text{jet}} = 5000$. They seeded the jet air with acetone and made LIF/PIV measurements of the scalar and velocity field. The Schmidt number of the system is 1.49. The tunnel cross-flow velocity profile has a peak value of $u_\infty = 2.95$ m/s. The jet nozzle is a simple pipe with 4.53 mm inner diameter and 320 mm length. In the absence of any cross-flow, fully developed pipe flow conditions are expected at the jet exit. The cross-flow is laminar and the 80% boundary layer thickness is $\delta = 1.32d$ at the location of the centre of the jet exit in absence of the jet.

The authors provide detailed experimental scalar profiles at a few vertical ($y/rd = 0.1$; 0.5; 1 and 1.5) and stream-wise stations ($x/rd = 0.5$, 1, 1.5 and 2.5) on the centre plane and off-centre measurement planes as a function of the non-dimensionalized stream-wise distance (x/rd, y/rd). Scalar field results are normalized by the scalar concentration value in the jet nozzle, C_0. For each image in the jet centre plane, $z = 0$, the jet potential core is in view and C_0 is determined directly. For the off-centre planes, Su & Mungal (2004) extrapolated known values from the $z = 0$ planes. As a consequence, only centre plane results can be compared.

Muppidi and Mahesh (2006-2007)[11,12] performed Direct Numerical Simulations (DNS) at conditions corresponding to the experiment of Su & Mungal (2004). Data is compared to the computed DNS results when available.

4.2 Test case of SPIV measurements

The SPIV measurements were performed in the Royal Military Academy (BE) laboratory in a blower-type low speed open-circuit wind tunnel. The tunnel cross-flow velocity profile had a peak value of $u_\infty = 2.5$ m/s. The jet nozzle is a simple pipe with inner diameter $d = 10$ mm. The average bulk jet velocity was $u_j = 2.2$ m/s. The momentum ratio based on the jet exit velocity profile is $r = 1.1$ and a Re_{jet} and

$Re_{\text{jet/freestream}}$ of approximately 1600. The laser sheet has been positioned on planes parallel to the 0-*x,y* plane (side view), containing the jet axis, on planes parallel to the 0-*y,z* plane (end view), featuring the CRVP and on planes parallel to the 0-*x,y* (top view). The image size in physical dimensions for all recording planes was approximately 50 × 35 mm. This yields a spatial resolution of about 1 mm.

5 COMPUTATIONAL METHOD

5.1 LES approach

In this effort, the LES calculations are performed with the CD-adapco STAR-CD 4.02 solver[13]. The current solver is valid for density-varying, non-isothermal, low-speed flows (free stream Mach number < 0.6). By applying Favre filtering to the Navier-Stokes equations, the momentum equation is recast in the following form:

$$\frac{\partial \overline{\rho}\langle u_i \rangle}{\partial t} + \frac{\partial \overline{\rho}\langle u_i u_j \rangle}{\partial x_j} = -\frac{\partial \overline{p}}{\partial x_i} + \frac{\partial \overline{\tau}_{ij}}{\partial x_j} \tag{2}$$

The effects of velocities not resolved by the computational grid are included by means of a subgrid-scale stress, which is defined as:

$$\tau_{SGS,ij} = \overline{\rho}\left(\langle u_i u_j \rangle - \langle u_i \rangle \langle u_j \rangle\right) \tag{3}$$

$\tau_{SGS,ij}$ is modelled using the Smagorinsky model and has the following form:

$$\tau_{SGS,ij} - \frac{2}{3} k_{SGS} \delta_{ij} = \overline{\rho} C_{s2} \Delta^2 \left|\overline{S}\right| \text{ where} \left|\overline{S}\right| = \sqrt{2\langle S_{ij} \rangle \langle S_{ij} \rangle} \tag{4}$$

The parameter C_{s2} is taken to be the square of the classic Smagorinsky constant $C_s = 0.18$.

By analogy, subgrid mixing is modelled by an eddy diffusitivity approach with a turbulent diffusitivity based on the turbulent viscosity of the subgrid stress model and a constant Schmidt number:

$$\overline{\rho}\left(\langle u_i Y_f \rangle - \langle u_i \rangle \langle Y_f \rangle\right) = \frac{\mu_t}{Sc} \frac{\partial \langle Y_f \rangle}{\partial x_i} \tag{5}$$

5.2 Grid characteristics and boundary conditions

The spatial discretization of the flow is based on structured meshes (Fig. 4).

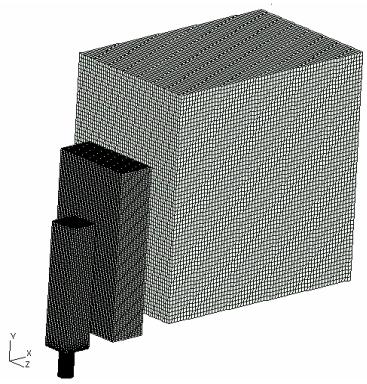

Figure 4: Generic mesh of the jet.

A multiple block approach, based on the Taylor microscales in the jet stream-wise and radial directions[14], is applied. The jet and cross-flow boundary layers were meshed first. Second, the jet was meshed and smoothly connected to the boundary layer grid. This core grid was allowed to grow linearly outwards at varying ratios. The grids are composed of 850000 and 600000 cells respectively, of which approximately 65% are placed on the jet.

Based on the analytical solution for the laminar boundary layer on a flat plate and the jet velocity profile, the cross-flow and jet boundary layer have a priori been meshed to resolve the flow down to the wall ($y^+ = 2$), ensuring that virtually all scales of the fluid motion are resolved and that the subgrid-scale contributions to the turbulent stresses are negligible near solid walls.

The flow in the main section and inflow for the pipe are driven by fixing the inflow velocity profiles while matching the experimental conditions. On the lateral and top surfaces, free-slip boundary conditions are prescribed, while on the bottom, a no-slip boundary condition is enforced. The inlet plane, lateral walls, and upper wall were all placed at distances that were judged to be sufficient to prevent the imposed boundary conditions from artificially constraining the solution. A pipe of length $2d$ is included in the computational domain, allowing the flow to develop naturally as the jet emerges into the cross-flow. The outflow condition is set to a zero gradient for all flow variables. A RANS simulation was run first and set as initial field for the LES simulations. No artificial vorticity is introduced in the domain. The instability of the free-stream and cross-flow mixing layer is expected to initiate the transient. Time advancement was implicit. The spatial and temporal discretizations are second–order accurate. The SIMPLE solution algorithm is used. The time step was optimized iteratively in order to achieve convergence at every time step with five outer iterations, leading to a time step in the order of $0.03d/u_\infty$. The solution is advanced in time to two flow-through times to allow the initial transients to exit the domain before computing time averaged statistics. Average quantities are measured over a time span of two flow-through times.

6 COMPARISONS TO EXPERIMENT

The numerical results of the SPIV and Su & Mungal test cases are compared to the experiments side by side. Throughout the rest of the paper, the experimental results of Su & Mungal are colored in red and the numerics are represented in blue. For the SPIV, the numerical results are overlaid in lines on experimental color maps.

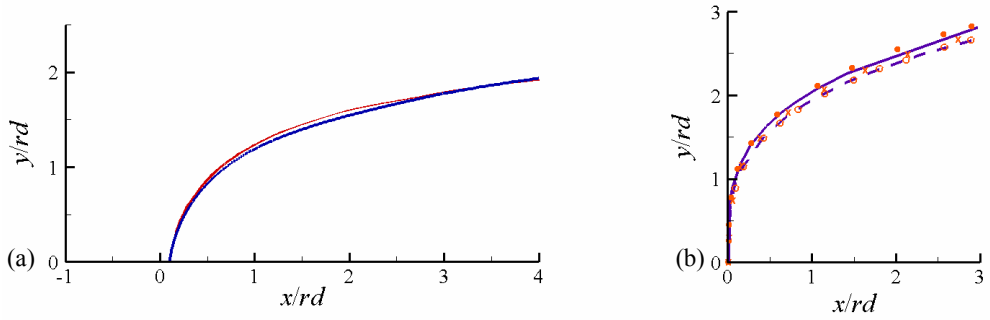

Figure 5: Comparison of jet trajectory: (a) SPIV: LES (–); Experiment (–); (b) Su & Mungal: LES (–); Experiment (•); DNS (×).

The jet trajectory is assessed first. The mean jet centre-lines are depicted in Fig. 5. For both cases, the trajectory slightly underestimates the experimental results. In the DNS computations, the under-shoot is even more pronounced. To place the mean trajectory of the jet, the centre-streamlines are included in all subsequent plots.

As the cross-flowing jet can be viewed as approximating a pure jet in its near field and a wake in its far field, the numerical results of the mean velocity field are assessed by the mean velocity magnitude $|\boldsymbol{U}|$ in the near filed (Fig. 6) and the mean cross-flow subtracted magnitude $|\boldsymbol{U}\text{-}U_\infty \mathbf{e}_y|$ in the far field (Fig. 7).

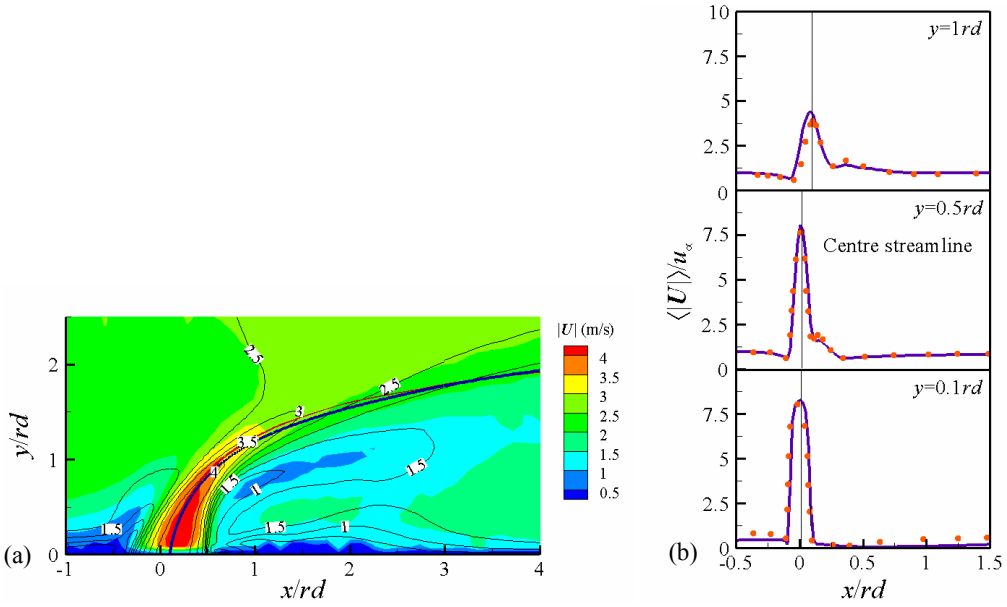

Figure 6: Comparison of mean velocity magnitude $|\boldsymbol{U}|$: (a) SPIV: LES (lines); Experiment (map); (b) Su & Mungal: LES (–); Experiment (•).

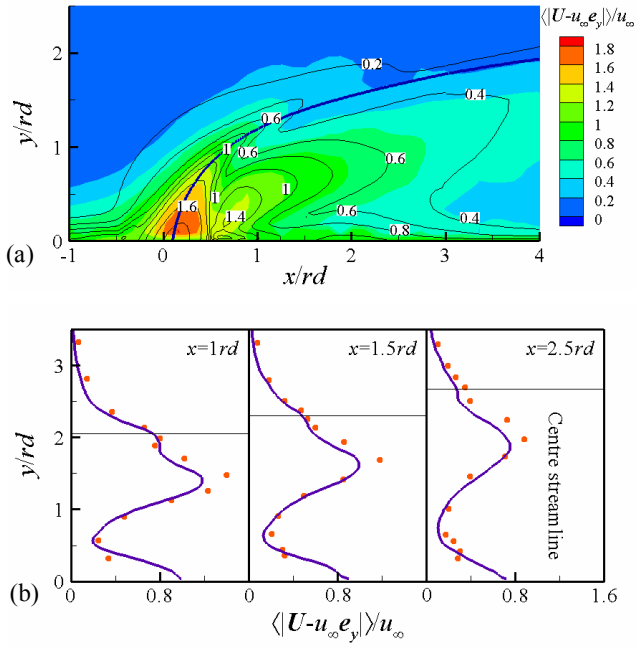

Figure 7: Comparison of mean cross-flow subtracted magnitude $|\boldsymbol{U}\text{-}U_\infty \mathbf{e}_y|$: (a) SPIV: LES (lines); Experiment (map); (b) Su & Mungal: LES (–); Experiment (•).

In the near field (Fig. 6) $|\boldsymbol{U}|$ is in good agreement. In the wake portion, the maximum $|\boldsymbol{U}-U_\infty \mathbf{e}_y|$ decays to fast. Therefore the LES appears to be to dissipative. This observation is congruent with results of Deardoff (1970) [15], stating that in the presence of mean shear, the standard C_s causes excessive damping.

The centre-plane turbulent resolved normal stress components are compared in Fig. 8.

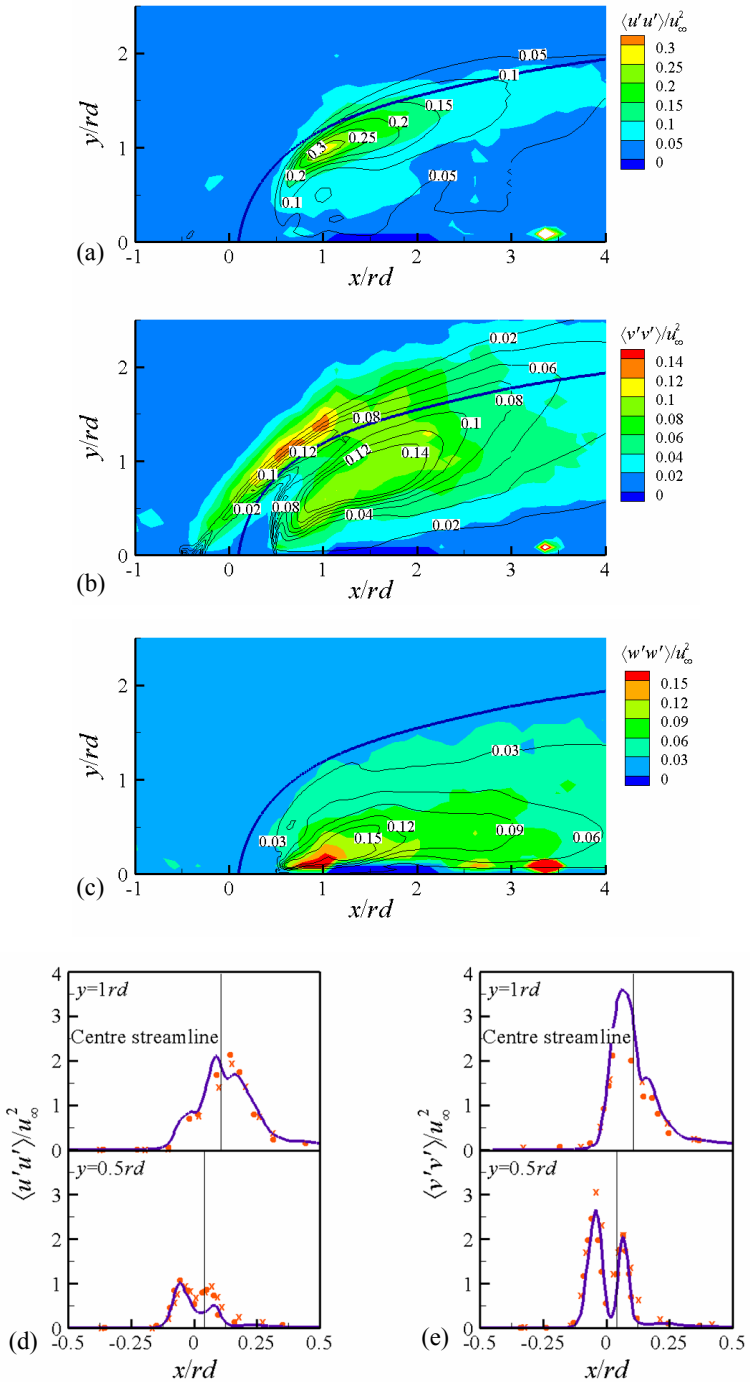

Figure 8: Comparison of turbulent normal stress components:
SPIV: (a) $\langle u'^2 \rangle$; (b) $\langle v'^2 \rangle$; (c) $\langle w'^2 \rangle$: LES (lines); Experiment (map)
Smith & Mungal: (d) $\langle u'^2 \rangle$; (e) $\langle v'^2 \rangle$: LES (–); Experiment (•); DNS (×).

As the LES filter width and the experimental spatial resolution differ, a one to one correlation does not hold. As a matter of fact the validation is of qualitative nature, as the LES turbulent stresses are expected to be larger in comparison with the experimental ones. Prior to assess the capability of the LES to reproduce $\langle u'^2 \rangle$, $\langle v'^2 \rangle$ and $\langle w'^2 \rangle$, one has to notice the difference in location of turbulence kinetic energy. For r = 5.7 the turbulence is most energetic near the jet exit. For r = 1 the regions of high $\langle u'^2 \rangle$, $\langle v'^2 \rangle$ and $\langle w'^2 \rangle$ are located predominantly in the region behind the jet.

For the flow case of Su & Mungal, fluctuations in the vertical direction at the jet exit inforce the hypothesis that the turbulence over the jet is generated by span-wise vortical structures. The roll-up of the jet shear layers begins to produce stream-wise fluctuations. At the y = 0.5 *rd* location, the windward peak of the averaged normal stress components $\langle v'^2 \rangle$ and $\langle u'^2 \rangle$ are well reproduced by the simulations. At the y = 1*rd* location, the higher $\langle v'^2 \rangle$ indicates large scale vortices that are formed periodically, with a reduced susceptibility to sporadic break-up into smaller scaled flow structures compared to the measurements. New, Lim & Luo (2006) [16] studied the influence of the jet velocity profile on the characteristics of a round JICF. As a result, they concluded, that there is an increase in jet penetration and a reduction in the near field entrainment of cross-flow with a parabolic JICF in comparison with the corresponding top hat JICF, where the shear layers are thinner. Those findings suggest that the pipe flow in the experiment is not fully turbulent. A jet velocity profile with thicker shear layers is less susceptible to instabilities, the shear layer will roll up in less energetic flow structures and the penetration will be higher. The discrepancy on the downwind side is not as conclusive. The lower peak in $\langle u'^2 \rangle$ at y = 0.5 *rd* suggests a delay in trailing edge vortices formation. The location of the maximum turbulence intensity y = 1*rd*, where the leading and trailing edge vortices collide, is well captured by the simulation.

For the SPIV flow case, no Kelvin-Helmholtz like instability, induced on the jet shear layer, is observed. The production of turbulence appears at $x \approx 1rd$ and $y \approx 1rd$. The turbulent kinetic energy at the jet centre-line is composed primarily by $\langle u'^2 \rangle$, suggesting a penetration of the cross-flow into the jet. $\langle v'^2 \rangle$ and $\langle w'^2 \rangle$ are located downstream of the edge of the jet, covering the entire lower part. These large co-located regions of $\langle v'^2 \rangle$ and $\langle w'^2 \rangle$ have the signature of a three-dimensional waving. On one hand, the regions of turbulent kinetic energy production are well reproduced. On the other hand, the normal stress components are overestimated by the LES. Although not quantifiable, the overestimation is in line with the smaller LES filter width compared to the experimental resolution.

As no experimental scalar data is available for r = 1, the capability of LES to reproduce the scalar field is limited to the test case of Su & Mungal. Figure 9 compares the mean and fluctuating scalar concentration in the near field. The profiles correspond to the symmetry-plane and to three vertical locations (y = 0.5, 1, and 1.5 *rd*). For the mean scalar field, a very good agreement is observed. For the fluctuating scalar field, the agreement appears reasonable at the first and third location, while there is some deviation between the simulation and the experiment at y = 1*rd*. At the jet exit, mixedness

$$MI = 1 - \langle C'^2 \rangle / \langle C \rangle \left(1 - \langle C \rangle\right) \tag{6}$$

is reproduced well, particularly seen in the context of the sharp gradients. At the y = 1*rd* location, while the location of the peaks appear to coincide, the peak magnitudes differ. Mixedness is underpredicted at the windward side and overpredicted at the downwind side. Unfortunately, no DNS data is available. The discrepancy on the windward side is in accordance with the computed stress components. The larger flow structures,

identified by the difference in $\langle v'^2 \rangle$, generate a higher entrainment and lower mixedness.

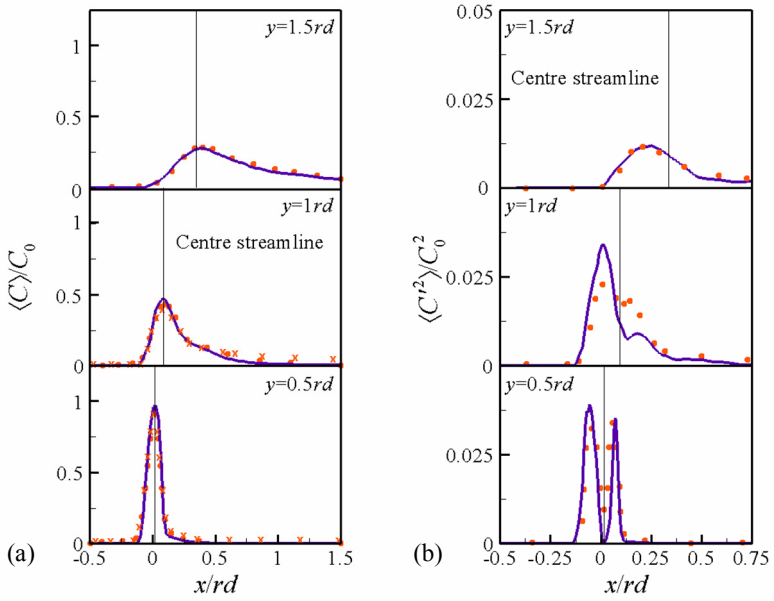

Figure 9: Comparison of mean and fluctuating scalar concentration in the near field: (a) Mean scalar field: LES (–); Experiment (•); DNS (×); (b) Averaged scalar variance: LES (–); Experiment (•).

The mean and fluctuating scalar concentration in the far field are compared in Fig. 10. The profiles correspond to the symmetry-plane, and to three stream-wise locations (x = 1, 1.5, and 2.5 *rd*).

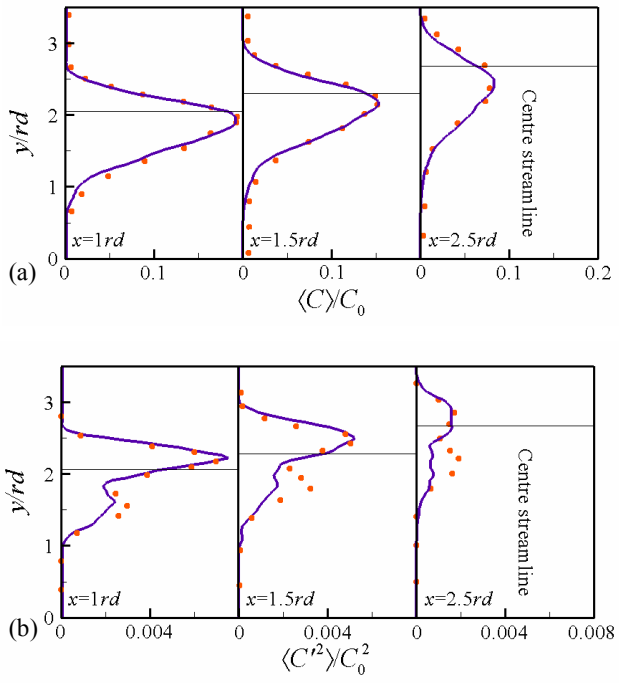

Figure 10: Comparison of mean and fluctuating scalar concentration in the far field: (a) Mean scalar field: LES (–); Experiment (•); (b) Averaged scalar variance: LES (–); Experiment (•).

As for the near field, the mean scalar field is in very good agreement. For the fluctuating scalar field, two distinct branches are observed. The upper branch reproduces well the downstream continuation of the mixing produced by the leading edge vortices. On the lower branch, the same trend as in the $y = 1rd$ near field shows up. Mixing produced by shear between the jet and the cross-flow and the intermittent CRVP is overpredicted. In the off centre profiles, Su & Mungal (2004) observe similar trends to those seen in the $z = 0$ plane, except that the wake-side variance peak is larger. At large z/rd values the wake-side variance peak becomes even larger than the windward side peak. Based on this trend, a slight off-centre measurement or slight off axis experimental set up would explain the difference in averaged scalar variation on the wake side. Smith & Mungal (1998) [17] highlighted those experimental difficulties in there end note: "*as a practical result, creating a transverse jet flow field that is symmetric about z = 0 is not regularly accomplished in laboratory studies*".

Overall, the agreement between simulations and experiments is quite good. Most discrepancies were identified and whether related to the computational method or uncertainties in the experimental set-up. An attempt could be made to adapt the model to the flow by adjusting the numerical constant C_{s2} of the Standard Smagorinsky model. With the view of an optimization on geometry and flow conditions, no case sensitive adaptation of C_{s2} was decided on. After successful assessment of the ability of LES to reproduce accurately the JICF flow physics, in the subsequent paragraph, the different vortical structures and their interaction will be looked into in more detail.

7 VORTICAL STRUCTURES

To better understand the formation of the vortical structures and the associated mixing, the mean field is analyzed first. The momentum ratio r independent flow features will be addressed briefly and the differences will be focused on. As the main focus is on mixing and the associated vortical structures, the horseshoe vortex and wake vortices, of minor importance, are left out in the analysis.

To illustrate the variety of different vortical structures, three flow quantities, pressure, vorticity and the second invariant of the mean velocity gradient tensor are examined. Pressure iso-surfaces mark the locations of low-pressure cores of vertical structures. Vorticity provides another mean of visualizing large-scale features in the flow field. To resolve whether a certain vorticity is due to a vortex or shear, the Q criterion technique (Hunt et al. (1988) [18]) in vortex identification is used. By evaluating the scalar

$$Q = R_{ij}R_{ij} - S_{ij}S_{ij} \tag{7}$$

with S_{ij} and R_{ij} the deformation and spin tensor respectively, high positive values of Q identify vortical flow regions where the rotation rate dominates the strain rate. Together, the three quantities provide a complete picture of the flow field.

Figure 11 shows mean flood w, with mean v black lines and red mean u lines in overlay, close to the jet exit $y = 0.3rd$. For clarity, the xz-plane is tilted under an angle of 45°. The view is completed by mean pressure iso-surfaces. Commonly agreed on in literature, the jet/cross-flow mixture converging upon the span-wise centre-line, and the reversed flow region, contributing to the high entrainment and mixedness in the downstream region, are identified for $r = 1$ and $r = 5.7$. The vortex core locations differ fundamentally. For $r = 5.7$, one sees a vortex sheet E extending from the windward side to the lateral edges of the jet. The vortex sheet results from the regular formation of span-wise rollers, in accordance with the $\langle v'^2 \rangle$ distribution in Fig. 8. No vortex sheet is

observed on the downwind side, indicating a more regular and earlier formation of vortices in the upstream shear layer in comparison with the downstream layer. For $r = 1$, three distinct flow structures appear in mean the flow field. Two steady "wake" vortex cores A are located immediately downstream on either side of the jet centre-line. To the authors' knowledge, these steady "wake" vortices are only reported by Peterson and Plesniak (2004) [19]. Conform to their nomenclature; these vortices will be referred to as downstream spiral separation node (DSSN) vortices for the remainder of the paper. Above the jet exit at $y = 0.3rd$ a hanging vortex B extends horizontally along the lateral edge of the jet. In hole vorticity is observed at position C.

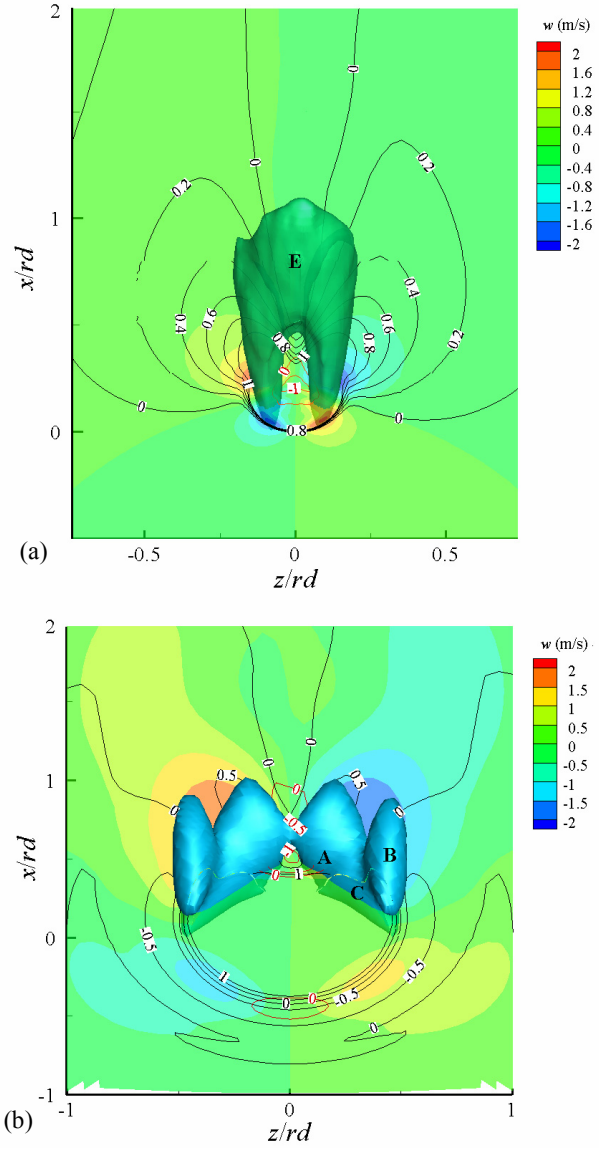

Figure 11: Mean velocity field and pressure iso-surface, $y = 0.3rd$: <w> (map); <u> (red lines); <v> (black lines). (a) $r = 5.7$. (b) $r = 1$

With the final perspective of optimizing the "Micromix" hydrogen combustion, the mean scalar mass fraction is overlaid by red lines of scalar mass fraction variance and black lines of *MI* (Eq. 6) in Fig. 12. For similarity, the x-position is scaled by rd, representing a yz-slice at a downstream position $x = 1.5rd$. For $r = 5.7$, the lateral

evolution of the mean fluctuating scalar concentration features a larger value with increasing off-centre position, reinforcing the hypotheses of a slight off-centre measurement or slight off axis experimental set up in the experiments by Su & Mungal (Fig. 10(b)), enhancing the validity of the LES. The benefit of mixing by JICF is completed by the apparent CRVP lifting wall fluid towards the jet. Meanwhile, constrained by a limited mean scalar sample size (64 samples in time) by the STAR-CD numerics, a bimodal scalar field with mass fraction peak values in side lobes can be identified. Furthermore, at equal mixing intensity, the mean fluctuating scalar concentration differs by an order of magnitude 10. The higher $\langle C'^2 \rangle$ at $r = 1$ indicates mixing by larger scale vortical structures compared to $r = 5.7$.

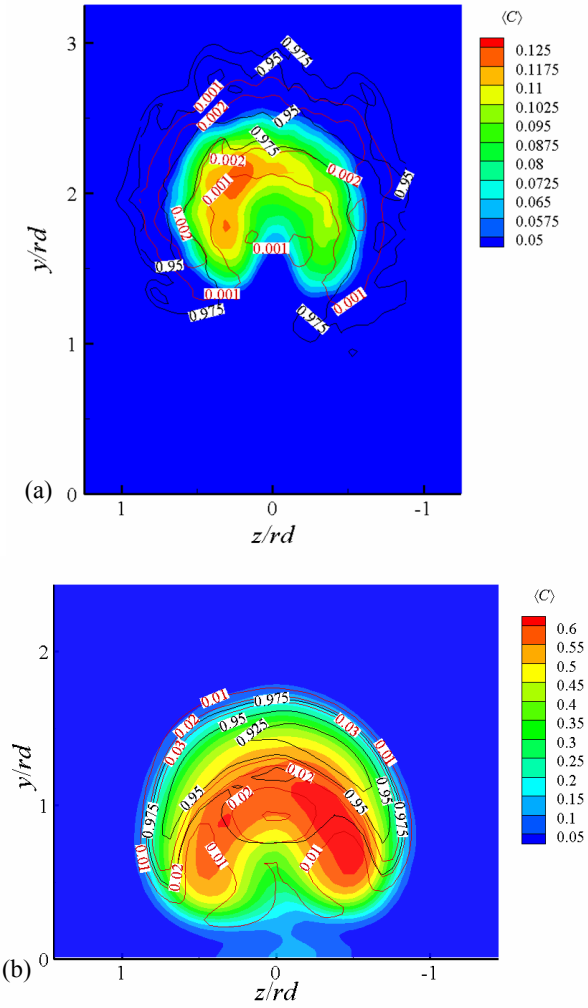

Figure 12: Mean scalar concentration, *MI* and mean fluctuating scalar concentration, $x = 1.5rd$: $\langle C \rangle$ (map); $\langle MI \rangle$ (red lines); $\langle C'^2 \rangle$ (black lines). (a) $r = 5.7$. (b) $r = 1$.

Pronounced branches of alternating low, high, low scalar concentration in the lower part of the $r = 5.7$ jet, suggest combustion physics similar to inverse triple flames. The significantly higher mean scalar concentration for $r = 1$ orients the flame structure to a diffusive type. On the one hand, though the considerably lower scalar concentration at $r = 5.7$, answers the need of higher mixing for optimum NO_x reduction, the benefit is overshadowed by the large span-wise spreading. The larger coverage will negatively affect the minimum distance for flame separation in between two injectors, reducing the

energy density. On the other hand, the large scale structures at $r = 1$ will result in sharp rises in concentration, resulting in small, distributed regions of high concentration fluid. These inhomogenities are prone to contribute to higher NO_x ppm's.

7.1 Flow physics for $r = 5.7$

Figure 13 gives a description of the hypothesized vortex tube model for $r = 5.7$. All vortex tubes (red, black and blue arrows numbered 1, 2 and 3 respectively) of the pressure iso-surface are believed to be vortices. As a vortex tube does not necessarily correspond to a vortex since vorticity in a vortex tube may be due to shear, consistency is obtained by z-vorticity in the centre-plane overlaid by a $+Q$ iso-line. Jet shear layer vortices, positively identified by the collocation of high vorticity and Q, appear on the upstream and leeward side. The upstream shear layer vortices (ULV) wrap around the jet, whereas the leeside shear layer vortices (LVL) remain in the jet core. The ULV and LVL "side arms" are tilted and roughly realign with the jet. Both vortex tubes are clearly identified as loops, rejecting the formation mechanism by evolving vortex rings proposed by Kelso, Lim & Perry (1995).

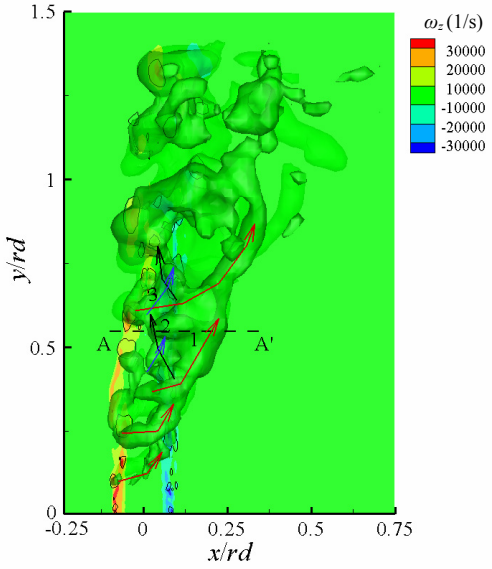

Figure 13: Instantaneous z-vorticity, Q iso-line and pressure iso-surface, centre plane, $r = 1$: ω_z (map); Q (lines).

To further analyze the highly three-dimensional flow field, instantaneous ω_y, ω_z and scalar concentration superposed by a $+Q$ iso-line at the AA' intersection $y = 0.55rd$ in Fig. 13. are reproduced in Fig. 14. The in-plane signature of the vortex tubes of Fig. 13 are identified by the corresponding numbers. Close to the centre-plane, the "side arms" of the UVL and LVL are in the z-direction (Fig. 14(a) 1, 2) and contribute mainly to ω_z. Bending towards the jet results in ω_y (Fig. 14(b) 1, 2). The UVL are believed to initiate the CRVP, as ω_y of the UVL and CRVP are of same rotation sign. The LVL, carrying ω_y of opposite sign, is the origin of a secondary CRVP (Fig. 14(b) 2) with rotation sense opposite to that of the primary CRVP (Fig 14(b) 1). Both CRVP coexist, leaving their trace in the scalar field (Fig. 14(c) 1, 2).

In addition to the span-wise rollers, vertical streaks (Fig. 13 blue arrows) are found in the main jet body. These streaks form when irregularities within a span-wise roller are stretched vertically by the local strain field. In Fig. 14(a) contours of ω_z appear in

several distinct structures indicated by number 3. In the gaps between these structures ω_y structures appear.

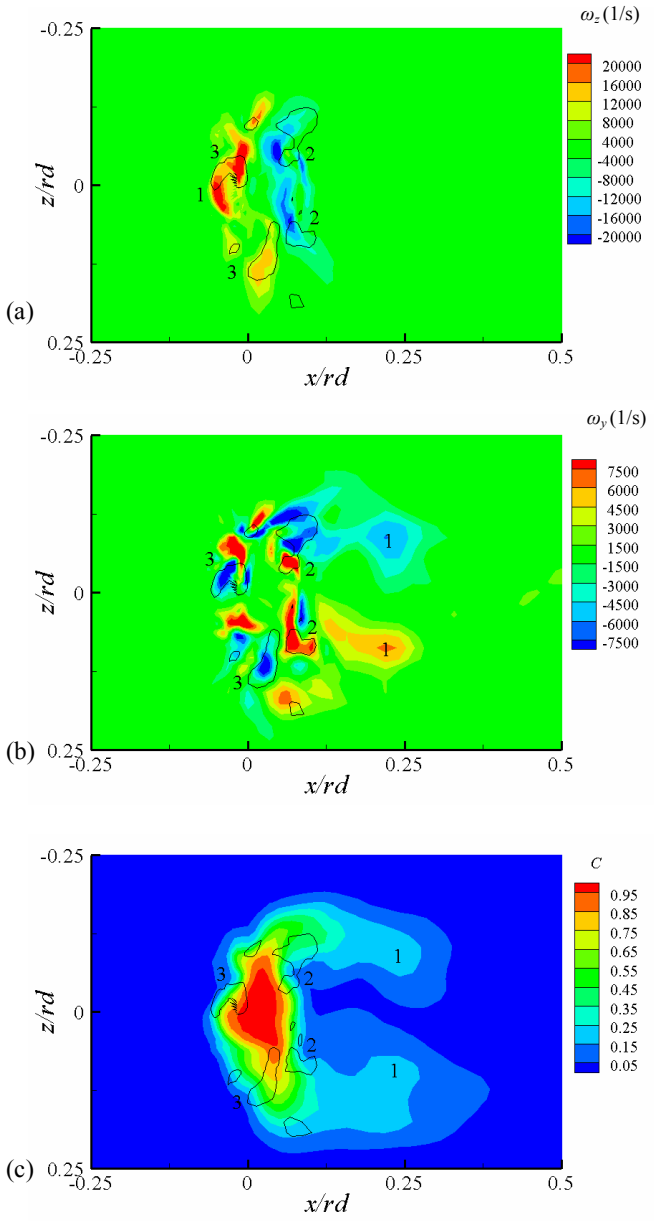

Figure 14: Instantaneous y,z-vorticity, scalar concentration and Q iso-line, $y = 0.55rd$, $r = 5.7$; (a) ω_z (map); Q (lines); (b) ω_y (map); Q (lines). (c) C (map); Q (lines).

7.2 Flow physics for $r = 1$

The near field flow structures and the formation of the CRVP will be looked into first. Afterwards the downstream evolution of the flow field will be developed step by step. In the near field, as expected, the topology of the mean pressure iso-surface (Fig. 11(b)), is found back in the instantaneous flow field in Fig. 15. The hanging vortex is a quasi-steady structure oscillating around a fixed location. The DSSN and in hole vortices behave in an unpredictable manner. At times they will shed into the mean flow, at other times they will shed vertical velocity. The effect of those vortices is visualized by two instantaneous streamlines and x-vorticity in a yz-plane at $x = 0.75rd$.

Streamline 1 originates from the cross-flow boundary layer upstream of the jet. Streamline 2 originates within the jet, close to the pipe wall. On the lateral edges a skewed mixing layer forms. Looking downstream, the direction of the fluid rotation ω_x is positive on the right hand side and of opposite sign on the left hand side. The fluid found in the hanging vortex originates from the free-stream, as indicated by streamline 1. Further evidence is given by the skink in the scalar profile in Fig. 16. Although deflected by the hanging vortex, the fluid stays initially closer to the wall. Further down-stream the fluid is drawn upwards by the CRVP, collecting in the ring like vortex tube labeled D, and forming a secondary CRVP on top of the primary CRVP, as shown later. The near wall counter-clock swirling channel fluid (streamline 2) collects in the DNSS, creating a path downstream for jet fluid (Fig. 16). The strong changes in the path of the upstream mark the start of vortex breakdown, resulting in realignment with the jet trajectory. Although weakened by the vortex breakdown, the primary CRVP appears to originate from the combined action of the in-hole vorticity and the DSSN, both carrying vorticity, the same sign as the CRVP.

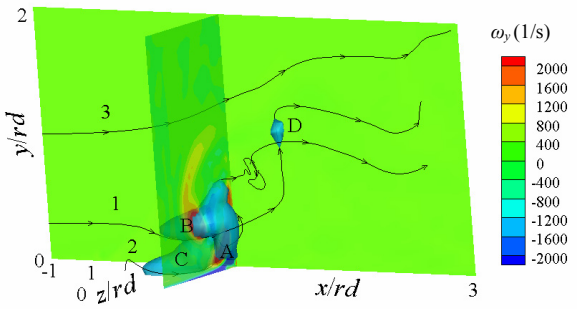

Figure 15: Instantaneous x-vorticity (map), $x = 0.75rd$, pressure iso-surface and streamlines, $r = 1$.

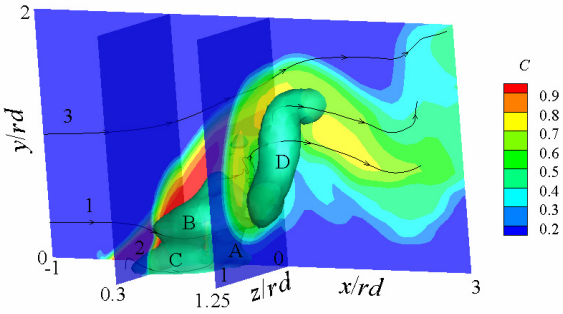

Figure 16: Instantaneous scalar concentration (map), centre plane, $x = 0.3rd$, $x = 1.25rd$, pressure iso-surface and streamlines, $r = 1$.

The evolution of the flow field will be addressed through mutual interpretation of Figures 17 and 18. On Fig. 17, the centre-plane is flood by w and the xz-plane $y = 1.25rd$ is mapped with v contours. Streamline 3, originating on the centre-plane upstream of the jet, visualizes a heavy cross-flow jet interaction. The cross-flow colliding upon the jet, forces the jet to spread. At position F in Fig. 17, the downward motion $w < 0$ and spreading $v > 0$ are clearly visible. The lifting action $w > 0$ of the CRVP enlarges the flow section, resulting in a lateral contraction $v < 0$ at position G. Repeated collisions between the cross-flow and the jet induce a three-dimensional waving, optically enhanced by streamlines 3 and 4 and the scalar concentration field in

Fig. 16. Those observations are consistent with the normal stress components in Fig. 8(a), (b), (c), spanning the entire wake region.

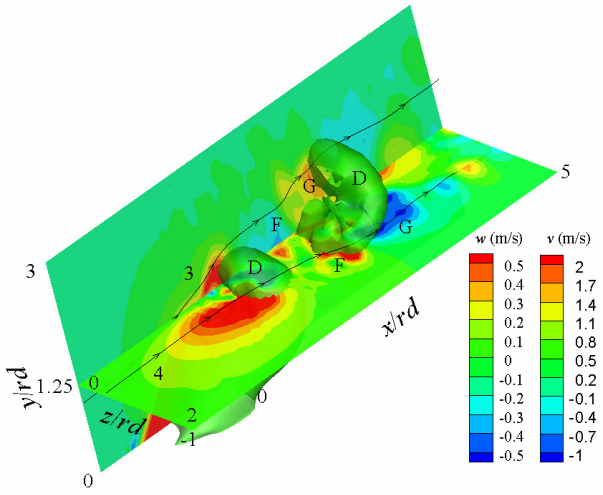

Figure 17: Instantaneous v (map), $y = 1.25rd$, instantaneous v (map), centre-plane, pressure iso-surface and streamlines, $r = 1$.

The z-vorticity field and Q distribution in Fig. 18 give insight into the RLV formation. The yz-plane locates the 0-y,z plane. Positive values of Q are colored in blue and regions of negative Q are represented in red. A vorticity sheet is observed to extend from the vicinity of the jet exit to about $2rd$ downstream. Beyond this location $+\omega_z$ jet like and $-\omega_x$ wake like structures alternate along the jet trajectory. The nature of the ω_z structures is assessed through the Q criterion and pressure iso-surface. On the one hand, the jet like structures coincide with $-Q$, identifying them as regions of local shear, induced by the cross-flow impacting on the jet. On the other hand, the $+Q$ and pressure iso-surface perfectly match and identify the rotational stream-tubes. Stream-tubes D, found on either side of the jet centre-plane, close on themselves under the influence of the jet meandering (Fig. 17). The wake like vorticity, congruent with the CRVP vorticity, strengthens the consistency of the proposed flow model.

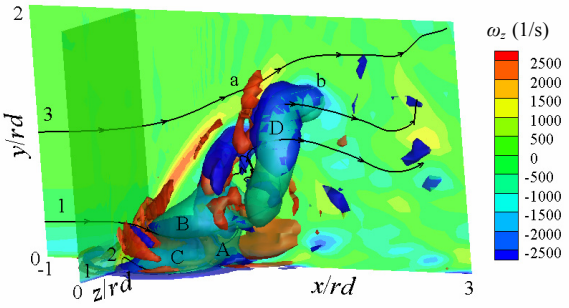

Figure 18: Instantaneous z-vorticity (map), centre-plane, pressure iso-surface, Q iso-surface and streamlines, $r = 1$.

Fig. 19 complements the mixing characteristics of low momentum JICF. Overall, the scalar concentration field features a "crankshaft" like topology. More specific, two separate mixing processes appear. As depicted in slice $x = 2rd$, a primary CRVP originates from the combined action of the in hole vorticity and the DSSN. Free-stream fluid, collecting in the RLV, generates a secondary CRVP (Fig. 19, slice $x = 3rd$), riding on top of the primary one. The coexistence of both CRVP ensures an intense mixing. Meanwhile, one has to be aware, that the mixing by large scale structures suffers from scalar concentration inhomogeneties (Fig. 12(b)). The benefits of mixing at low momentum ratio $r = 1$, with respect to a reduction in NO_x emissions, stays an open question for the time being.

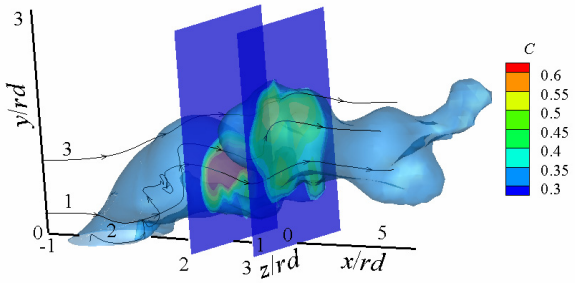

Figure 19: Instantaneous scalar concentration, $x = 2rd$, $x = 3rd$, scalar concentration iso-surface and streamlines, $r = 1$.

8 CONCLUSIONS

In the present work, the case of a jet exhausting in a cross-stream at low $r = 1$ and medium $r = 5.7$ momentum ratio at respective Reynolds number ($Re_j \approx 1600$ and 5000) has been analyzed numerically. The ability of the commercial CFD code STAR-CD, with the Standard Smagorinsky model, to reproduce the JICF complex flow field, was successfully assessed by comparison to experiments. Minor discrepancies were identified and related to uncertainties in the experimental set-up or computational shortcomings. With the focus on the mixing characteristics, the driving vortical structures and their interaction were looked into, and kinematically consistent vortex models are proposed. For $r = 5.7$, the destabilization is induced by Kelvin-Helmholtz instabilities on the shear layer. The dominant downwind vortical structures roll up, wrap around the jet and tilt. Evolving open loops are identified to initiate the CRVP. For $r = 1$, the mechanism differs fundamentally. The cross-flow collides with the jet, inducing a three-dimensional waving. In addition to the primary CRVP, originating from in hole and DSSN vortices, ring like structures and a secondary CRVP on top of the primary CRVP form. With prospect of optimizing the "Micromix" combustion principle, the higher mixedness at $r = 5.7$, in comparison with $r = 1$, prevails. The benefit is overshadowed by a larger jet spreading scaling with rd. As a matter of fact, the optimization of the "Micromix" combustion principle by means of r stays an open question. Future combustion simulations are expected to give a clear answer.

REFERENCES

[1] A. Westernberger, *Liquid Hydrogen Fuelled Aircraft – System Analysis*, 5th Framework program of the European Communities, 2000
[2] G. Dahl, F. Suttrop, Engine Control and Low-NOx Combustion for Hydrogen Fuelled Aircraft Gas Turbines, *Int. J. Hydrogen Energy*, **Vol. 23**, No. 8, pp. 695-704, 1998
[3] A. Robinson, U. Rönna, H. Funke, Development and testing of a 10 kW diffusive micromix combustor for hydrogen-fuelled μ-scale gas turbines, *ASME Turbo Expo*, 2008
[4] T.H. New, T.T. Lim, S.C. Luo, Effects of jet velocity profiles on a round jet in cross-flow, *Experiments in Fluids*, **Vol. 40**, pp. 859-875, 2006
[5] R.M. Kelso, T.T. Lim, A.E. Perry, An experimental study of round jet in cross-flow, *J. Fluid Mechanics*, **Vol. 306**, pp. 111-144, 1995
[6] J. Andreopoulos, W. Rodi, Experimental investigation of jets in a cross-flow, *J. Fluid Mechanics*, **Vol. 138**, pp. 93-127, 1984
[7] L. L. Yuan, R. L. Street, J. H. Ferziger, Large-eddy simulations of a round jet in crossflow, *J. Fluid Mechanics*, **Vol. 379**, pp. 71-104, 1999
[8] T. T. Lim, T. H. New, S. C. Luo, On the development of large-scale structures of a jet normal to a cross flow, *Physics of Fluids*, **Vol. 13**, N° 3, pp. 770-775, 2001
[9] R. Camussi, G. Guj, A. Stella, Experimental study of a jet in a crossflow at very low Reynolds number, *J. Fluid Mechanics*, **Vol. 454**, pp. 113-144, 2002
[10] L.K. Su, M.G. Mungal, Simultaneous measurements of scalar and velocity field evolution in turbulent cross-flowing jets, *J. Fluid Mechanics*, **Vol. 513**, pp. 1-45, 2004
[11] S. Muppidi, K. Mahesh, Passive scalar mixing in jets in cross-flow, *44th Aerospace Sciences Meeting and Exhibit*, AIAA, 2006
[12] S. Muppidi, K. Mahesh, Direct numerical simulation of round turbulent jets in crossflow, *J. Fluid Mechanics*, **Vol. 574**, 2007, pp. 59-84
[13] STAR-CD 4.02 User's guide, CD-adapco, 2006
[14] E. Recker, W. Bosschaerts, P. Hendrick, Large eddy simulation of mixing in a round jet in crossflow, *39th AIAA Fluid Dynamic conference*, Jun 2009
[15] J. W. Deardorff, A numerical study of three-dimensional turbulent channel flow at large Reynolds numbers, *J. Fluid Mechanics*, **Vol. 41**, pp. 453-480, 1970
[16] T.H. New, T.T. Lim, S.C. LUO, Effects of jet velocity profiles on a round jet in cross-flow, *Experiments in Fluids*, **Vol. 40**, pp. 859-875, 2006
[17] S. H. Smith, M.G. Mungal, Mixing, structure and scaling of the jet in cross-flow, *J. Fluid Mechanics*, **Vol. 357**, pp. 83-122, 1998
[18] J.C.F. Hunt, A.A. Wray, P. Moin, Eddies, stream and convergence zones in turbulent flows, *Report CTR-S88*, Center for Turbulence Research, NASA-Ames Research Center and Standford University, California, USA
[19] S. D. Peterson, M.W. Plesniak, Evolution of jets emanating from short holes into crossflow, *J. Fluid Mechanics*, **Vol. 503**, pp. 57-91, 2004